

Supplementary Information

A. Datasets summary

For OCT movie acquisitions, there was an average interval between return from spaceflight and postflight acquisition of 11.5 ± 10.2 days (the minimum interval was 3 days, and the maximum was 35 days).

A datasets summary table is provided below.

Table S1. Datasets summary table. The table provides characteristics of OCT videos and volumes.

	dataset 1	dataset 2
dataset name	space macular videos	space macular volumes
subjects	13 astronauts	6 astronauts
sex	9 males, 4 females	5 males, 1 female
age [yo \pm SD]	46.8 ± 8.9	47.5 ± 9
timepoints (L launch, R return, m month, d day)	2 (pre-, post- spaceflight)	4-6 (L-21 to 18 m, L-9 to 6 m, L+30 d, L+90 d, R-30 d, R+1 to 3 d)
eyes	OU	OU
# scans/eye [videos OR volumes]	1-5 videos	1-2 volumes
scan size [px \times px]	768×496	512×496
approximate horizontal resolution [$\mu\text{m}/\text{px}$]	11	11
approximate vertical resolution [$\mu\text{m}/\text{px}$]	3.9	3.9
approximate physical area [mm \times mm]	8.4×1.9	5.6×1.9
# frames per scan [B-scans]	441 (average)	97 or 193
# frames total for the dataset	45,439	11,719

B. Post-processing

Post-processing of the deep learning choroid segmentation output mask first consists of applying an opening operation to minimize undesirable false positive regions. Opening is performed for 5 iterations using a 5 pixels width \times 3 pixels height rectangular kernel. To accurately identify Bruch's membrane (BM) and the choroid-sclera interface (CSI) as the upper and lower choroid boundaries, respectively, including when several isolated false positive regions are present, the binary image undergoes a series of boundaries extraction steps:

The first boundaries extraction step consists of iterating through each of the mask's objects to obtain images of the BM and CSI candidate segments. For each object, the contour is obtained and any void inside the region is filled. An argmax function is applied in the vertical axis direction to obtain locations of the BM candidate segments. BM candidate segments are then combined into a single binary image. Any candidate pixel at the top edge of the BM candidate segments image is removed, and candidate segments less than 10 pixels in size are discarded. Similar processing is performed to obtain the CSI candidate segments image, removing any candidate pixels at the bottom image edge instead of at the top edge.

The second boundaries extraction step consists of connecting boundary paths for both the BM and CSI candidate segments images. In both cases, an iteration through all candidate segments is performed to identify right and left segment extremities and their coordinates. Each extremity is connected to its closest opposite side extremity, or to the opposite edge of the image where crossing with an existing segment does not occur. Once extremities are connected, only the largest connected region in the boundary candidate segments image is kept. Then, the extremities connections process is performed once more to ensure the remaining region connects with the left and right edges of the image.

For the single remaining region in each boundary candidate segments image, the shortest path between the left and right edge of the image is determined and all other pixels are discarded. To prevent the BM and CSI from crossing each other, if any BM location is found at a lower location than the corresponding CSI location along the vertical axis of both boundary candidate segments images, then the BM location is changed to one pixel above the corresponding CSI location. The BM and CSI are each returned as arrays of locations along the vertical axis of their respective candidate segments images.

Algorithm 1 Side points iteration (e. g. right side, P_2)

```
1: for every point  $P_i$  do
2:   gather all left-side extremities on right side of current extremity ( $P_2$ )
3:   opposite candidate points array,  $A_o = [7, 9, 11, 13, 15, 17]$ 
4:   gather all right-side extremities on right side of current extremity ( $P_2$ )
5:   edge most points array,  $A_e = [6, 4, 8, 10, 12, 14, 16, 18]$ 
6:   if  $A_o$  is not empty then
7:     obtain list of distances from current point to opposite side candidate points
8:     distances array,  $A_d = [10, 34, 52, 41, 58, 62]$ 
9:     while  $A_d$  not empty do
10:      gather point coordinate corresponding to minimum distance in  $A_d$  ( $P_7$ )
11:      connect minimum distance point ( $P_7$ ) to current extremity ( $P_2$ )
12:      if no line crossing
13:        and line vertical distance < than fraction of image height
14:        and line horizontal distance < than fraction of image width then
15:          draw line in the image
16:        end while loop
17:      else
18:        remove current distance from  $A_d$ 
19:        continue while loop
20:      end if
21:    end while [ $A_d$  not empty]
22:  else if  $A_o$  is empty
23:    and  $A_e$  is empty then
24:      current extremity is edge most,
25:      connect current extremity directly horizontally to the same side image edge
26:    end if
27: end for
```

Figure S1. Side points iteration algorithm. Pseudocode of the side points iteration algorithm.

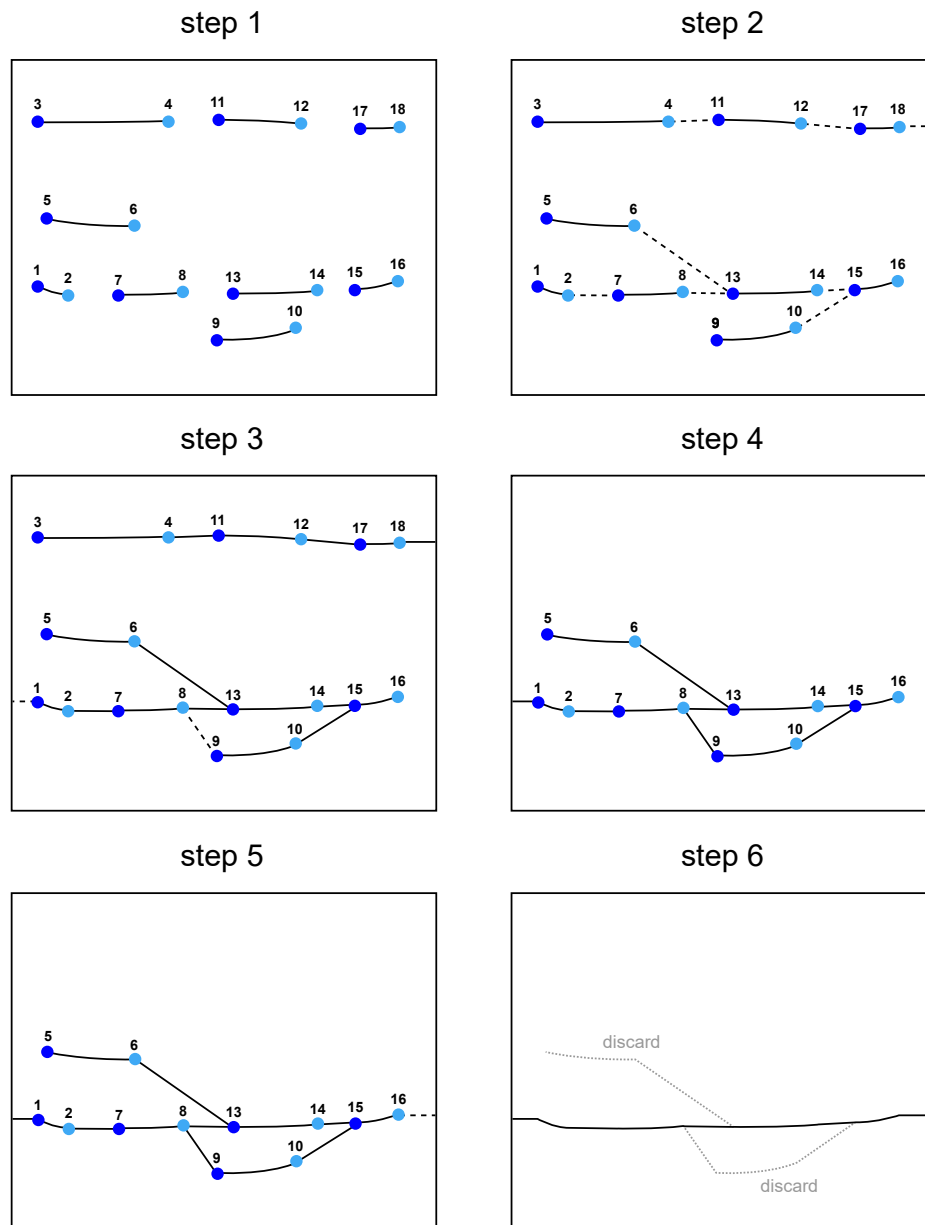


Figure S2. Illustrated post-processing steps. (step 1) Boundary candidate points identification. (step 2) Side points iteration for right side points. (step 3) Repetition of side points iteration for left side points. (step 4) Only the largest region of interest in the image is kept. (step 5) Repetition of side points iteration for right and left sides to ensure image side edges connections. (step 6) Only the shortest path between image right and left side edges is kept.

C. Space macular videos and volumes choroid segmentation cross-validation and post-processing results

Equations relating to the inaccurate segmentation criterion are provided below

$$CT_{B\text{-scan mean}} = \frac{\sum_{i=1}^n CT_{B\text{-scan column}, i}}{n} \quad (1)$$

$$PC_{CT\text{ diff}} = \frac{|CT_{\text{manual}} - CT_{\text{model}}|}{CT_{\text{manual}}} \times 100\% \quad (2)$$

$$C_{\text{inaccurate}} = \begin{cases} 1 & \text{if } PC_{CT\text{ diff}} \geq 20\%, \\ 0 & \text{otherwise.} \end{cases} \quad (3)$$

where $CT_{B\text{-scan column}}$ is choroid thickness corresponding to a column in a B-scan image, $CT_{B\text{-scan mean}}$ is the mean of all column choroid thicknesses in a B-scan, $PC_{CT\text{ diff}}$ is the absolute difference between $CT_{B\text{-scan mean}}$ obtained through manual segmentation, CT_{manual} , and $CT_{B\text{-scan mean}}$ obtained through automated segmentation, CT_{model} , as a percentage of CT_{manual} , and $C_{\text{inaccurate}}$ is the inaccurate segmentation criterion.

Equations relating to the segmentation failure criterion are provided below

$$CT_{B\text{-scan max}} = \max_{1 \leq i \leq n} \{CT_{B\text{-scan column}, i}\} \quad (4)$$

$$PC_{\text{max } CT\text{ diff}} = \frac{|CT_{B\text{-scan max}} - CT_{\text{manual}}|}{CT_{\text{manual}}} \times 100\% \quad (5)$$

$$C_{\text{failure}} = \begin{cases} 1 & \text{if } PC_{\text{max } CT\text{ diff}} \geq 60\% \text{ and } \sigma_{\text{model}} \geq 2.5 \cdot \sigma_{\text{manual}}, \\ 0 & \text{otherwise.} \end{cases} \quad (6)$$

where $CT_{B\text{-scan max}}$ is the maximum choroid thickness of all column choroid thicknesses in a B-scan, σ_{model} is the standard deviation of a set of $CT_{B\text{-scan column}}$ obtained through automatic segmentation, σ_{manual} is the standard deviation of a set of $CT_{B\text{-scan column}}$ obtained through manual segmentation, $PC_{\text{max } CT\text{ diff}}$ is the absolute difference between $CT_{B\text{-scan max}}$ and CT_{manual} as a percentage of CT_{manual} , and C_{failure} is the segmentation failure criterion.

Figure S3 displays 5-fold cross-validation choroid segmentation performance results for space macular videos and volumes. Figure S4 depicts 5-fold cross validation post-processing results for space macular videos and volumes. As shown on the left side of figure S4a, higher fold-averaged $PC_{\text{max } CT\text{ diff}}$ values indicate a higher occurrence of failed segmentations in the absence of post-processing. Similarly, the stacked bar plots on the left side of figure S4b indicate that images were more likely to meet the inaccurate segmentation and segmentation failure criteria for a given fold in the absence of post-processing. The same analysis for the macular volumes dataset, as shown in S4d and e, suggests that images in that dataset were less problematic.

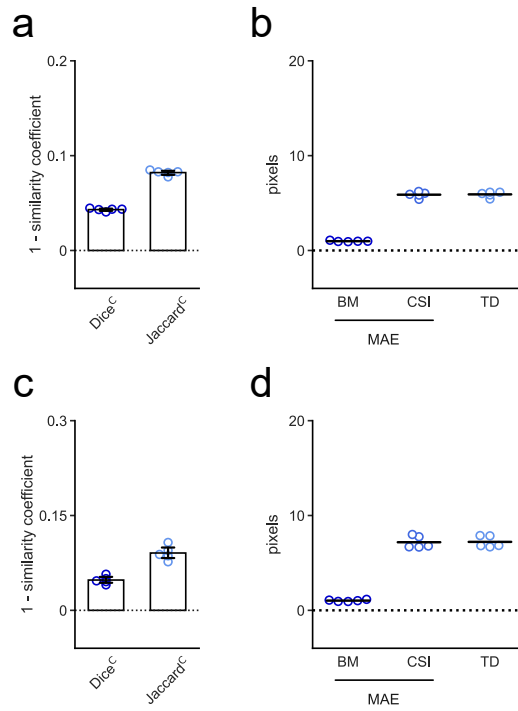


Figure S3. 5-fold cross-validation choroid segmentation performance results for space macular videos and volumes. (a) Dice^C and Jaccard^C results for the test set of 5-fold cross-validation space macular videos-retrained models. (b) BM and CSI layers mean absolute error, and thickness difference for the test set of 5-fold cross-validation space macular videos-retrained models (c) Dice^C and Jaccard^C results for the test set of 5-fold cross-validation space macular volumes-retrained models. (d) BM and CSI layers mean absolute error, and thickness difference for the test set of 5-fold cross-validation space macular volumes-retrained models.

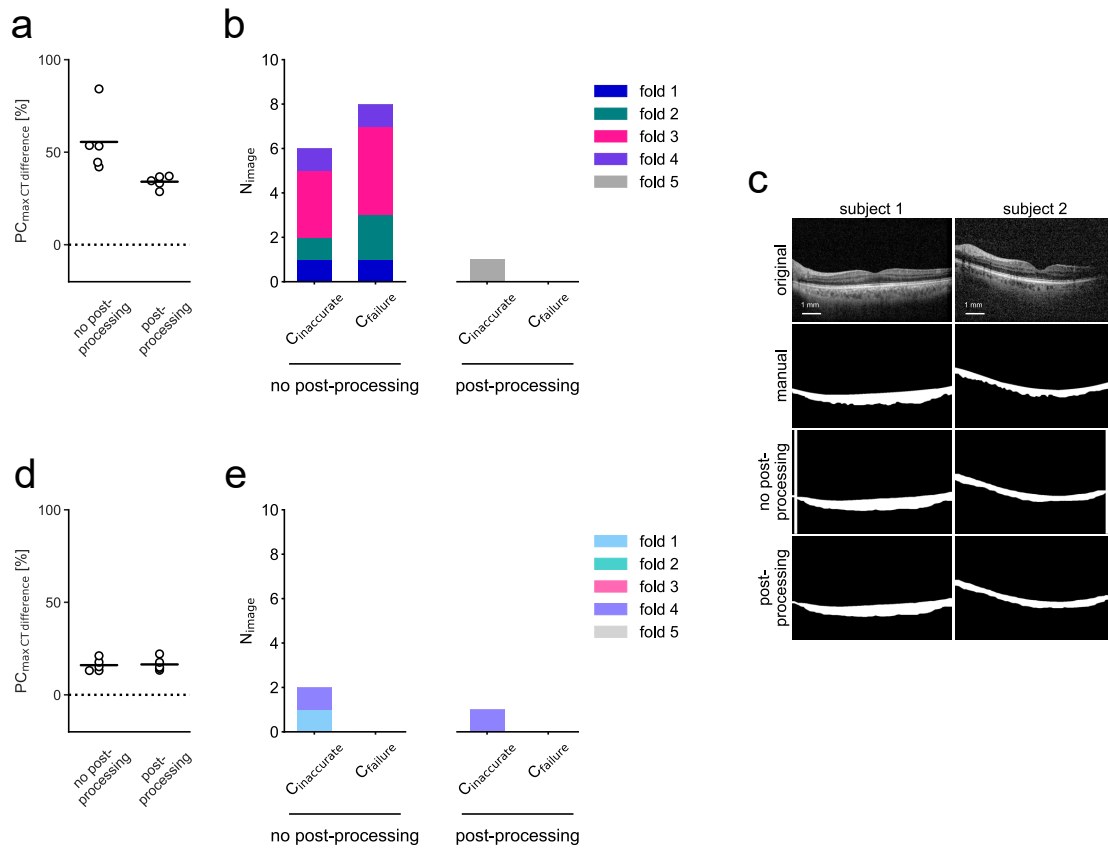


Figure S4. 5-fold cross-validation post-processing results for space macular videos and volumes. (a) PC_{max CT} diff 5-fold cross-validation results without and with post-processing for choroids segmented using OCT videos-retrained models. (b) Stacked bar charts of inferred choroid segmentations (left) without and (right) with post-processing meeting inaccurate segmentation and segmentation failure criteria for 5-fold cross-validation OCT videos-retrained models. (c) Original B-scans and binary choroid segmentation masks for 2 subjects obtained manually, through model inference without and with post-processing. Binary choroid segmentation masks for which post-processing was not applied show segmentation failures. (d) PC_{max CT} diff 5-fold cross-validation results without and with post-processing for choroids segmented using OCT volumes-retrained models. (e) Stacked bar charts of inferred choroid segmentations (left) without and (right) with post-processing meeting inaccurate segmentation and segmentation failure criteria for 5-fold cross-validation OCT volumes-retrained models.

D. Luminal area processing

Individual B-scan processing to obtain a binary mask of luminal area and towards performing CVI calculation were implemented similarly as described in literature^{1; 3; 2}. First, Niblack local thresholding was applied in Python (v3.10.0) through `sckit-image` (0.19.2). The Niblack function was implemented with a specified window of 35 pixels and a constant value, k , of 0.8. Following Niblack local thresholding, dilation and closing morphological operations, both using a 3×3 pixels kernel, were applied to the image. The final binarized luminal area image was achieved by keeping only the processed region corresponding to the choroid layer. The CVI for individual B-scans is obtained through the following equation

$$CVI = \frac{LA}{CA} \quad (7)$$

where LA is luminal area and CA is total choroid area. The CVI for OCT volumes is obtained through the following equation

$$CVI = \frac{LT}{CT} \quad (8)$$

where LT is luminal thickness averaged over the specified macular region, and CT is choroid thickness averaged over the specified macular region.

E. ETDRS subfields

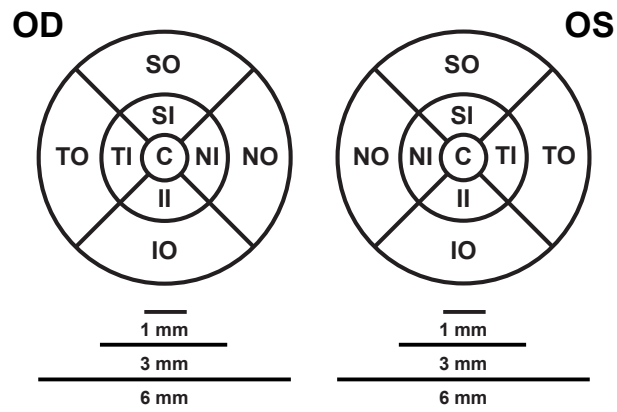


Figure S5. ETDRS subfields. Nine ETDRS subfields for right eye (OD) and left eye (OS). (C center, SI superior inner, NI nasal inner, II inferior inner, TI temporal inner, SO superior outer, NO nasal outer, IO inferior outer, TO temporal outer).

F. Transforms implementation details

The Lomb–Scargle periodogram and Lomb–Scargle spectrogram were implemented in Python (v3.10.0) through SciPy (1.8.0). At the specified automatic real time frame averaging of 5 frames, the OCT device used had an approximate acquisition rate of 21.662 frames/second (0.0462 seconds period). For the spectrogram, a 40 elements window (~ 1.848 seconds) was used with a 2 elements step (~ 0.0924 seconds).

As shown in figure S6, peaks at the specified sinusoid frequency are visible in the Lomb–Scargle periodogram. For the Lomb–Scargle spectrogram, the peaks are sustained over the time interval.

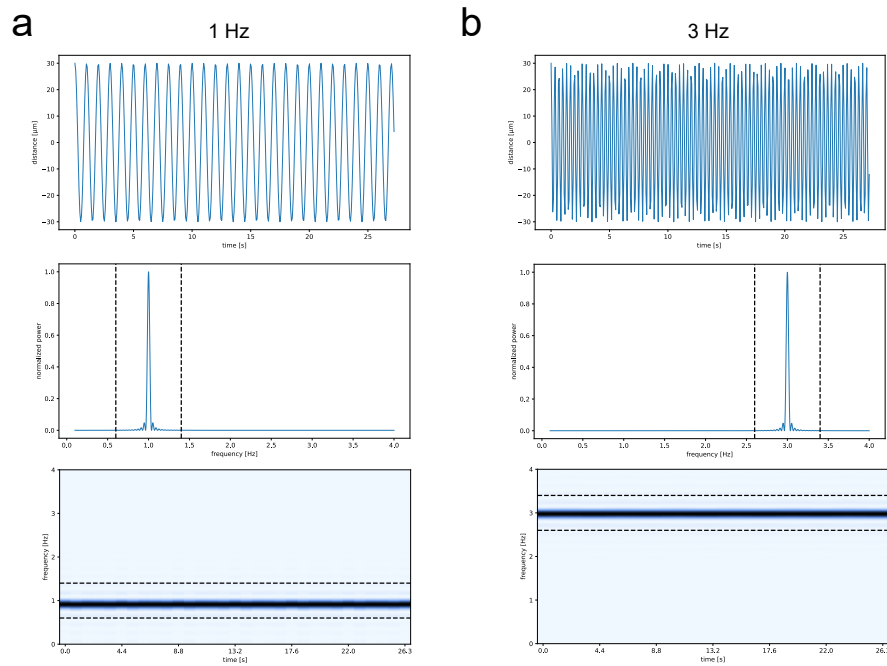


Figure S6. Transforms calibration. (a) Transforms calibration with a 1 Hz sinusoid. Top row features a sinusoidal timeseries, second row features the Lomb–Scargle periodogram and third row features the Lomb–Scargle spectrogram. Dashed line on the Lomb–Scargle periodogram and Lomb–Scargle spectrogram show values $\pm 40\%$ of the specified frequency value. (b) Transforms calibration with a 3 Hz sinusoid.

G. Scheme for volumes manual labelling

		OD																			
		1	2	3	4	5	6	7	8	9	10	11	12	13	14	15	16	17	18	19	20
L - 21 to 18 m	1	x	x						x	x											
L - 21 to 18 m	2		x	x						x	x										
L - 9 to 6 m	1			x	x						x	x									
L - 9 to 6 m	2				x	x						x	x								
L + 30 d	1					x	x						x	x							
L + 30 d	2						x	x						x	x						
L + 90 d	1							x	x						x	x					
L + 90 d	2								x	x						x	x				
R - 30 d	1									x	x						x	x			
R - 30 d	2										x	x						x	x		
R + 1 to 3 d	1											x	x						x	x	
R + 1 to 3 d	2												x	x						x	x

		OS																			
		1	2	3	4	5	6	7	8	9	10	11	12	13	14	15	16	17	18	19	20
L - 21 to 18 m	1	x	x						x	x											
L - 21 to 18 m	2		x	x						x	x										
L - 9 to 6 m	1			x	x						x	x									
L - 9 to 6 m	2				x	x						x	x								
L + 30 d	1					x	x						x	x							
L + 30 d	2						x	x						x	x						
L + 90 d	1							x	x						x	x					
L + 90 d	2								x	x						x	x				
R - 30 d	1									x	x						x	x			
R - 30 d	2										x	x						x	x		
R + 1 to 3 d	1											x	x						x	x	
R + 1 to 3 d	2												x	x						x	x

Figure S7. Scheme for volumes manual labelling. Dataset 2 volumes manual labelling scheme. (L launch, R return, m months, d days).

H. Additional choroid layer segmentation and lumen segmentation performance evaluation

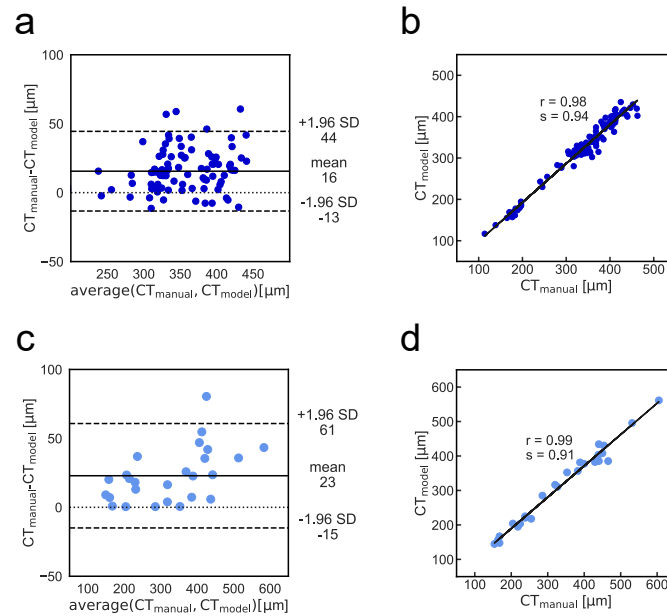


Figure S8. Choroid layer segmentation additional performance evaluation. (a) Bland-Altman plot illustrating the agreement between CT obtained manually and through model inference for the OCT videos test set. (b) Scatterplot and regression line of model inferred CT against manually obtained CT for the OCT videos test set. r Pearson correlation coefficient, s regression line slope. (c) Bland-Altman plot illustrating the agreement between CT obtained manually and through model inference for the OCT volumes test set. (d) Scatterplot and regression line of model inferred CT against manually obtained CT for the OCT volumes test set. r Pearson correlation coefficient, s regression line slope.

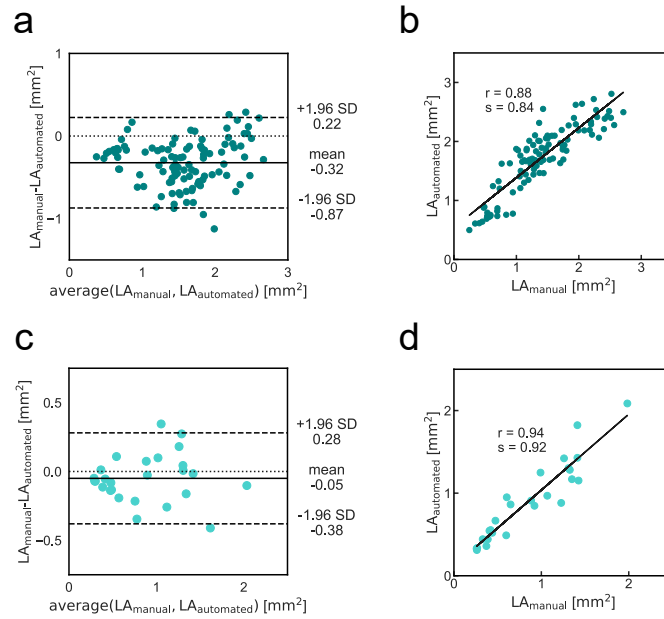


Figure S9. Choroid lumen segmentation additional performance evaluation. (a) Bland-Altman plot illustrating the agreement between LA obtained manually and LA obtained automatically for the OCT videos test set. (b) Scatterplot and regression line of automatically obtained LA against manually obtained LA for the OCT videos test set. r Pearson correlation coefficient, s regression line slope. (c) Bland-Altman plot illustrating the agreement between LA obtained manually and LA obtained automatically for the OCT volumes test set. (d) Scatterplot and regression line of automatically obtained LA against manually obtained LA for the OCT volumes test set. r Pearson correlation coefficient, s regression line slope.

I. Pre-spaceflight and post-spaceflight temporal quantification difference plots

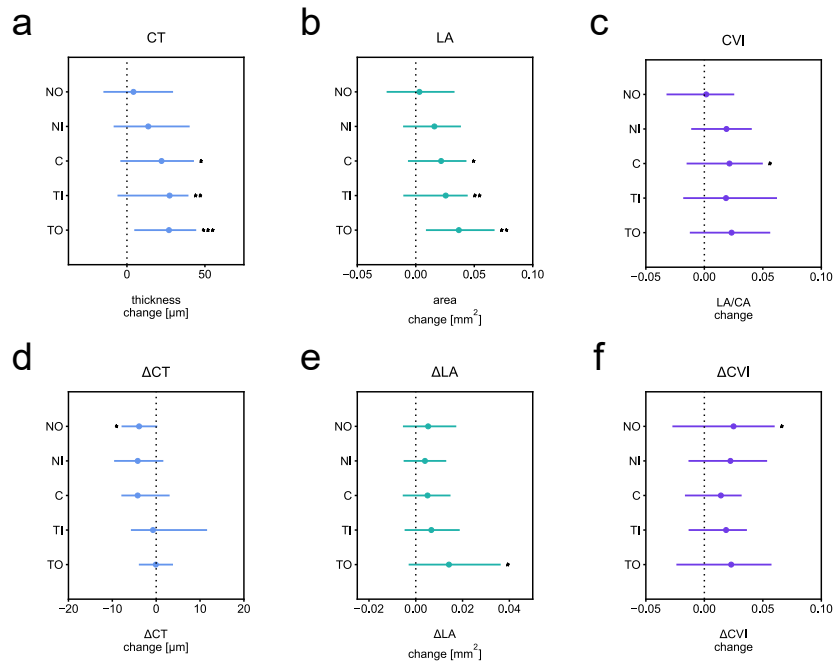


Figure S10. Pre-spaceflight and post-spaceflight temporal quantification difference plots. (a) Difference plot between post- and preflight CT measurements averaged over the selected segments for all astronaut eyes. Cross-sectional ETDRS subfield differences are shown. Difference plot lines represent the difference interquartile range and dots show the mean difference. (b) Difference plot between post- and preflight LA measurements. (c) Difference plot between post- and preflight CVI measurements. (d) Difference plot between post- and preflight ΔCT corresponding to the selected segments. (e) Difference plot between post- and preflight ΔLA . (f) Difference plot between post- and preflight ΔCVI . * $P < 0.05$, ** $P < 0.01$, *** $P < 0.001$, linear mixed model.

J. Pre-spaceflight and post-spaceflight sample timeseries and transforms

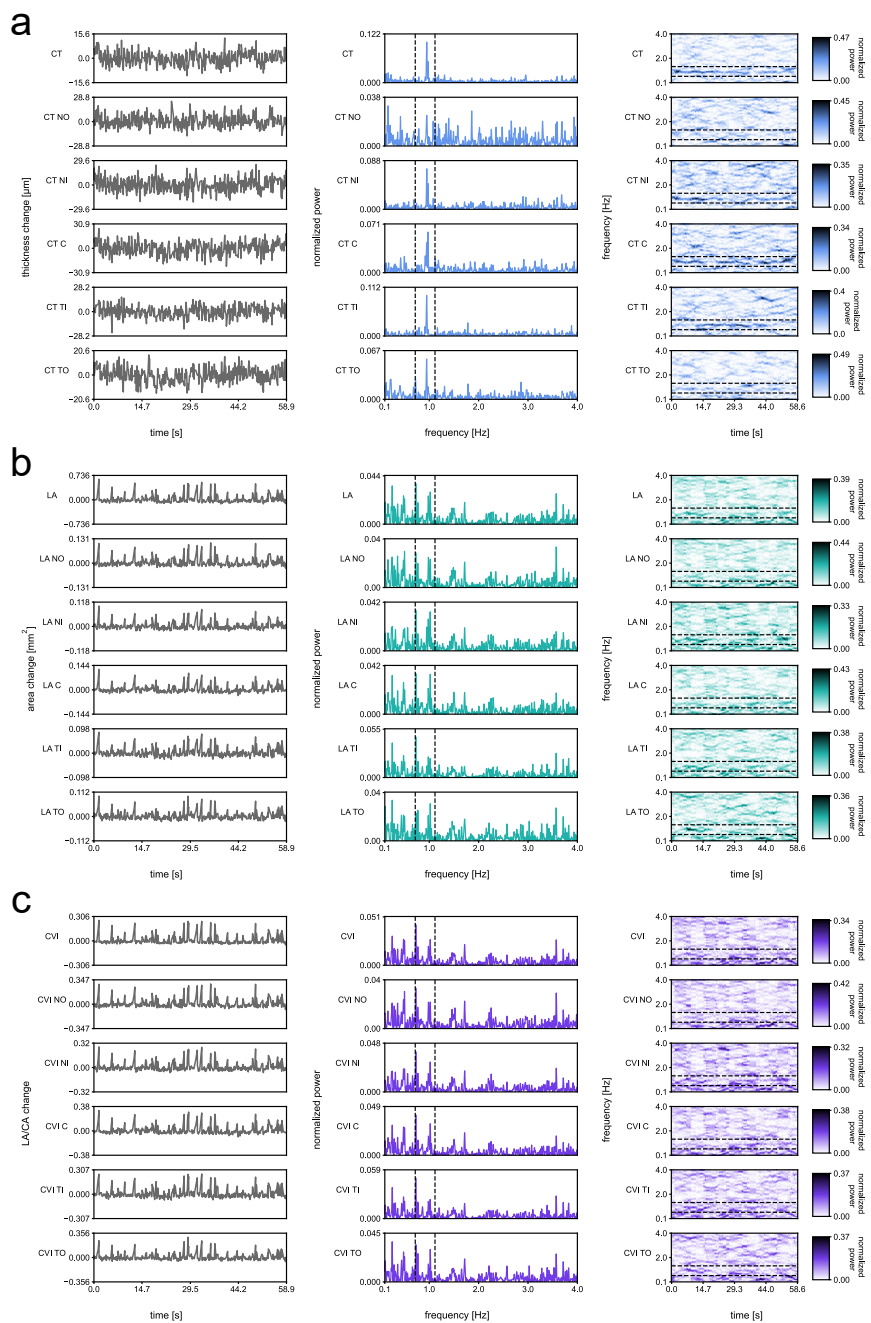


Figure S11. Pre-spaceflight sample timeseries and transforms. (a) Pre-spaceflight CT selected segment timeseries, frequency and joint time-frequency transforms for one subject's eye acquisition. First column features selected segment timeseries, second column features Lomb–Scargle periodograms and third column features Lomb–Scargle spectrograms. Dashed lines on the Lomb–Scargle periodogram and Lomb–Scargle spectrogram show values $\pm 20\%$ and $\pm 40\%$ of the oximeter measured heart rate value, respectively. (b) Pre-spaceflight LA selected segment timeseries, frequency and joint time-frequency transforms for the same subject's eye acquisition. (c) Pre-spaceflight CVI selected segment timeseries, frequency and joint time-frequency transforms for the same subject's eye acquisition.

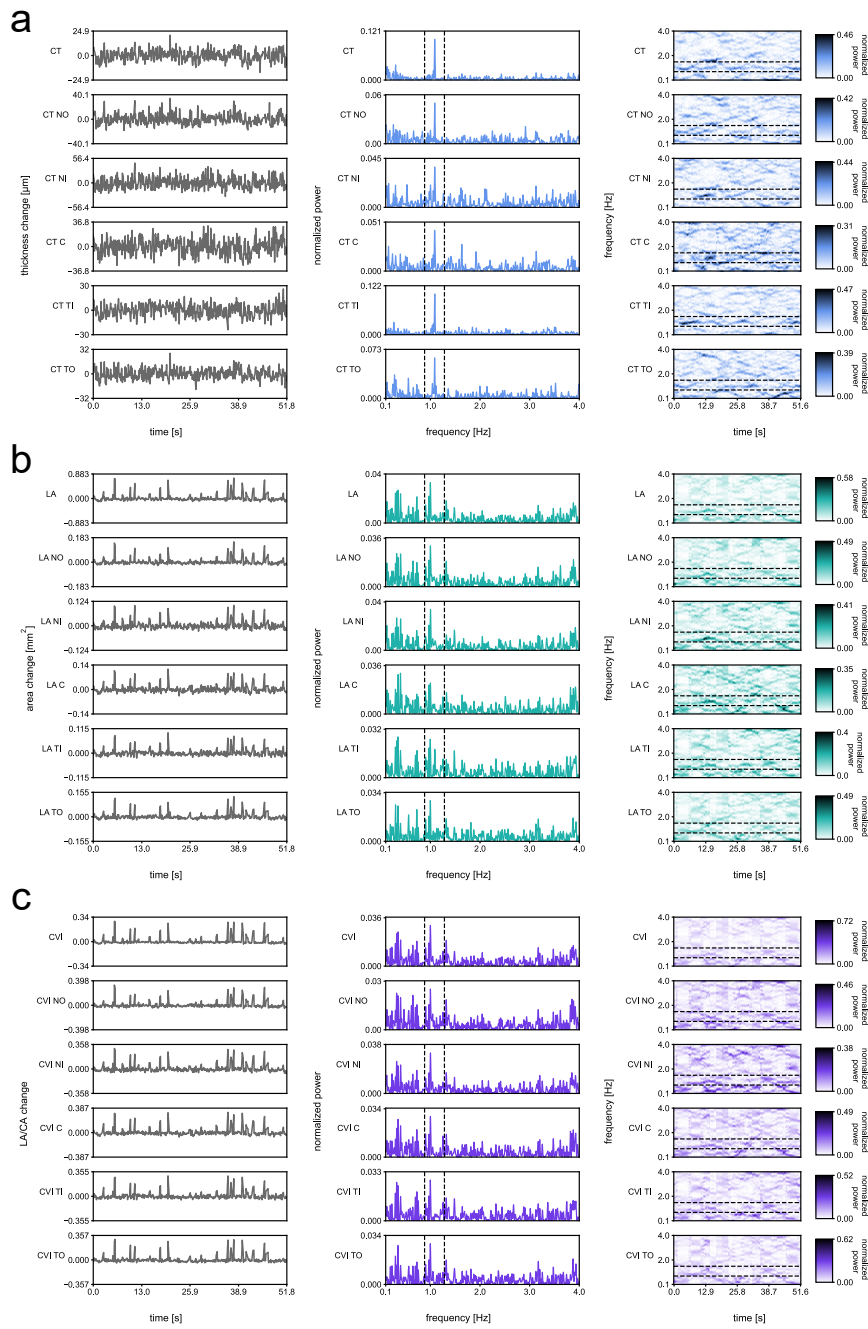


Figure S12. Post-spaceflight sample timeseries and transforms. (a) Post-spaceflight CT selected segment timeseries, frequency and joint time-frequency transforms for one subject's eye acquisition. First column features selected segment timeseries, second column features Lomb–Scargle periodograms and third column features Lomb–Scargle spectrograms. Dashed lines on the Lomb–Scargle periodogram and Lomb–Scargle spectrogram show values $\pm 20\%$ and $\pm 40\%$ of the oximeter measured heart rate value, respectively. (b) Post-spaceflight LA selected segment timeseries, frequency and joint time-frequency transforms for the same subject's eye acquisition. (c) Post-spaceflight CVI selected segment timeseries, frequency and joint time-frequency transforms for the same subject's eye acquisition.

K. Additional spatial changes

One or both eyes from all 6 subjects were represented in at least one preflight timepoint ($n_{\text{eye}} = 10$, $n_{\text{subject}} = 5$ for launch - 21 to 18 months; $n_{\text{eye}} = 11$, $n_{\text{subject}} = 6$ for launch - 9 to 6 months). Not all eyes from all six subjects were available for individual inflight and postflight timepoints. When obtaining the significance of differences between individual inflight and postflight timepoint quantifications and their preflight baseline, if an eye was represented in both preflight timepoints, the two preflight quantification values were averaged. Quantification values corresponding to the available eyes for individual inflight and postflight timepoints were then compared with the preflight baseline ($n_{\text{eye}} = 11$, $n_{\text{subject}} = 6$ for launch + 30 days; $n_{\text{eye}} = 10$, $n_{\text{subject}} = 5$ for launch + 90 days; $n_{\text{eye}} = 6$, $n_{\text{subject}} = 3$ for return - 30 days; $n_{\text{eye}} = 10$, $n_{\text{subject}} = 5$ for return + 1 to 3 days).

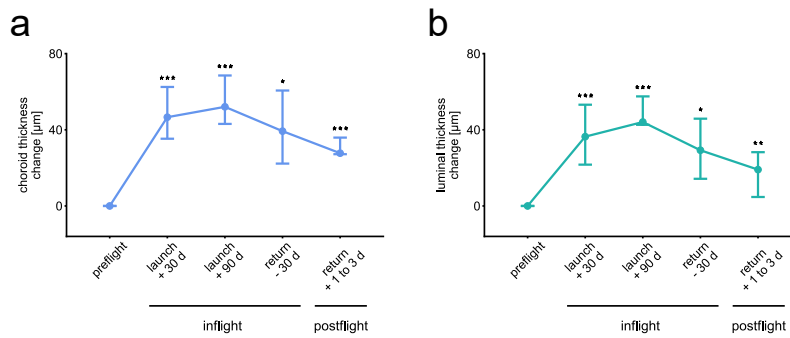


Figure S13. Spatial OCT choroid thickness changes. (a) Line chart of change in CT over averaged preflight, inflight and postflight timepoints for all astronaut eyes. Error bars show the difference interquartile range and dots show the mean difference. (b) Line chart of change in LT over averaged preflight, inflight and postflight timepoints for the same eyes. (d days). *P < 0.05, **P < 0.01, ***P < 0.001, linear mixed model.

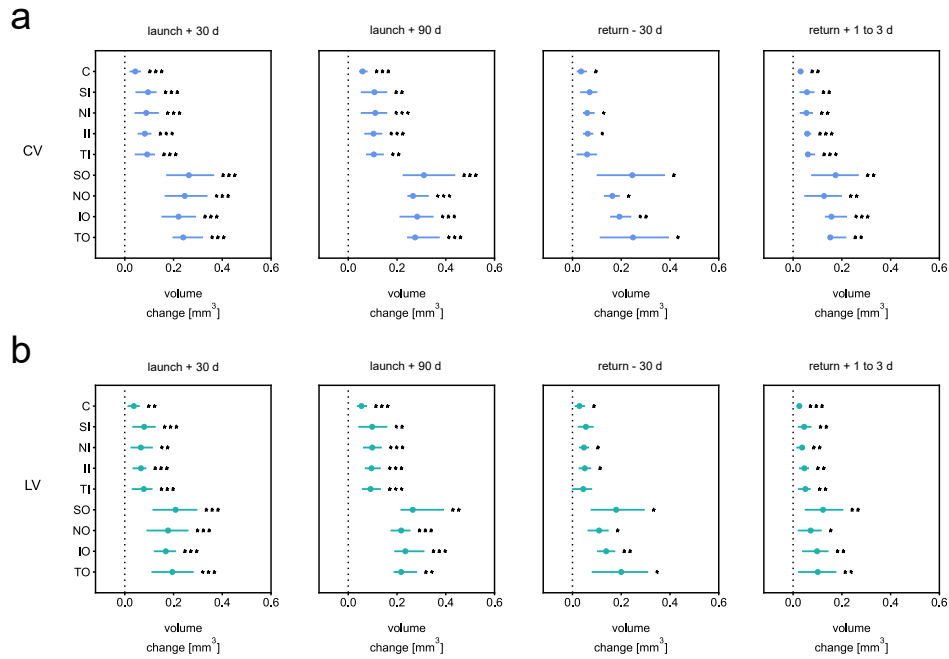


Figure S14. Spatial quantification choroid volume difference plots. (a) Difference plots between several timepoints and preflight CV measurements over the specified macular regions for all astronaut eyes. ETDRS subfield differences are shown. Difference plot lines represent the difference interquartile range and dots show the mean difference. (b) Difference plot between several timepoints and preflight LV measurements. (d days). *P < 0.05, **P < 0.01, ***P < 0.001, linear mixed model.

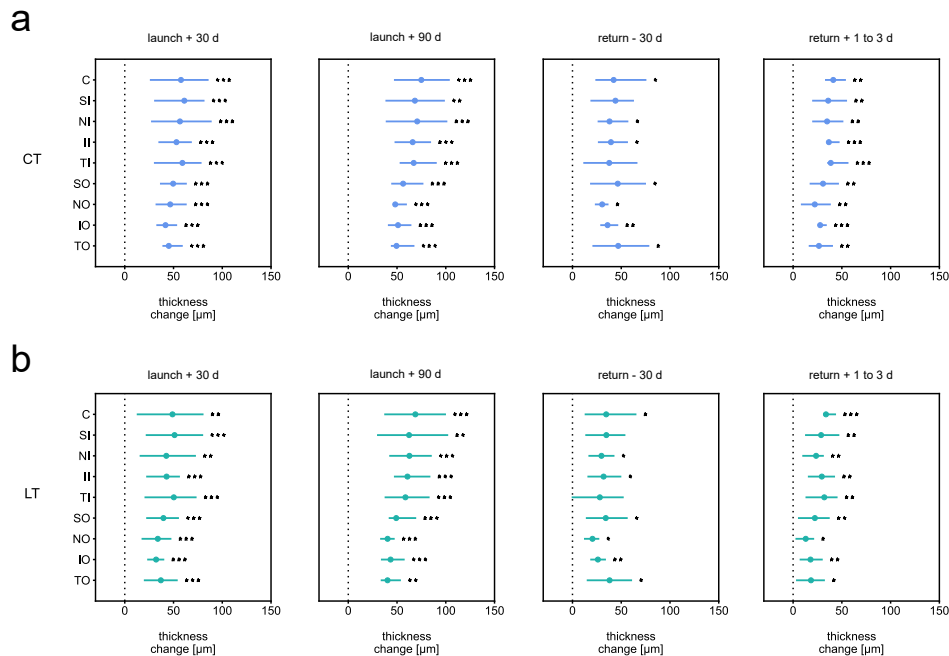


Figure S15. Spatial quantification choroid thickness difference plots. (a) Difference plots between several timepoints and preflight CT measurements averaged over the specified macular regions for all astronaut eyes. ETDRS subfield differences are shown. Difference plot lines represent the difference interquartile range and dots show the mean difference. (b) Difference plots between several timepoints and preflight LT measurements. (d days). *P < 0.05, **P < 0.01, ***P < 0.001, linear mixed model.

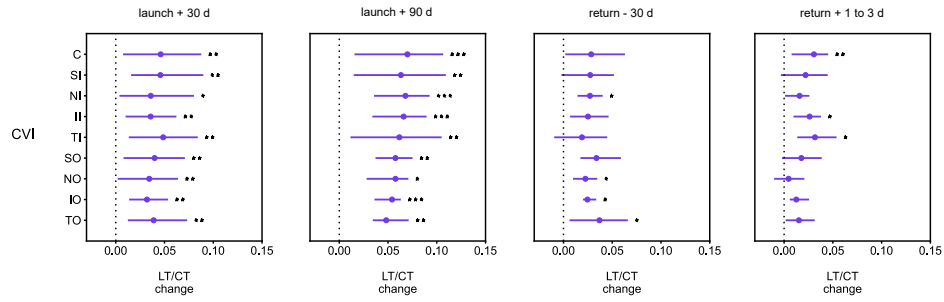


Figure S16. Spatial quantification CVI difference plots. Difference plots between several timepoints and preflight CVI measurements averaged over the specified macular regions for all astronaut eyes. ETDRS subfield differences are shown. Difference plot lines represent the difference interquartile range and dots show the mean difference. (d days). * $P < 0.05$, ** $P < 0.01$, *** $P < 0.001$, linear mixed model.

L. Pre-spaceflight spatial changes

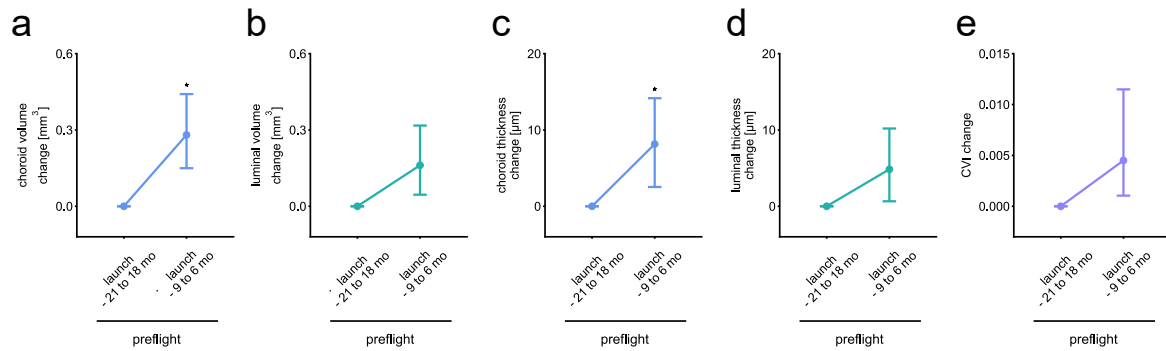


Figure S17. Pre-spaceflight spatial OCT choroid changes. (a) Line chart of change in CV over preflight timepoints for all OCT volumes astronaut eyes. Error bars show the difference interquartile range and dots show the mean difference. (b) Line chart of change in LV. (c) Line chart of change in CT. (d) Line chart of change in LT. (e) Line chart of change in CVI. (d days). *P < 0.05, linear mixed model.

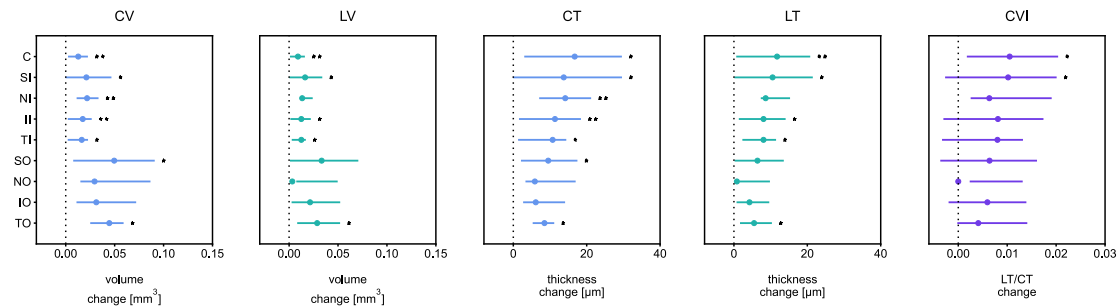


Figure S18. Pre-spaceflight spatial quantification difference plots. Difference plots between preflight timepoints CV and LV measurements over the specified macular regions, and CT, LT and CVI measurements averaged over the specified macular regions for all astronaut eyes. ETDRS subfield differences are shown. Difference plot lines represent the difference interquartile range and dots show the mean difference. *P < 0.05, **P < 0.01, linear mixed model.

M. Quantification tables

Table S2. OCT videos quantification table. Quantification values for OCT videos at the preflight timepoint (average \pm standard deviation).

	CT [μm]	ΔCT [μm]	LA [mm^2]	ΔLA [mm^2]	CVI	ΔCVI
global	297.3 \pm 85.3	16.274 \pm 6.256	1.62 \pm 0.58	0.2235 \pm 0.0872	0.6048 \pm 0.0693	0.0849 \pm 0.0406
NO	271.6 \pm 96.2	21.7 \pm 10.45	0.247 \pm 0.12	0.0446 \pm 0.0256	0.5826 \pm 0.084	0.0911 \pm 0.0422
NI	351.6 \pm 115.2	30.975 \pm 15.419	0.231 \pm 0.099	0.0422 \pm 0.0164	0.6348 \pm 0.0877	0.097 \pm 0.041
C	375.6 \pm 121.4	33.748 \pm 16.962	0.251 \pm 0.105	0.0448 \pm 0.0163	0.6403 \pm 0.0984	0.0977 \pm 0.0403
TI	361.2 \pm 112.4	31.472 \pm 18.029	0.24 \pm 0.096	0.0419 \pm 0.0165	0.6439 \pm 0.0873	0.0925 \pm 0.0374
TO	315.7 \pm 95.7	24.938 \pm 14.005	0.287 \pm 0.107	0.0524 \pm 0.0216	0.5951 \pm 0.0697	0.0977 \pm 0.0449

Table S3. OCT volumes quantification table. Quantification values for OCT volumes at the preflight timepoint (average \pm standard deviation).

	CV [mm^3]	LV [mm^3]	CT [μm]	LT [μm]	CVI
global	10.7893 \pm 2.8846	5.2799 \pm 2.1061	309.2 \pm 75.6	150.7 \pm 54.9	0.4743 \pm 0.0623
C	0.2792 \pm 0.0739	0.1495 \pm 0.0619	355.5 \pm 94.8	190.4 \pm 79.4	0.5135 \pm 0.0936
SI	0.555 \pm 0.135	0.2997 \pm 0.1139	351.5 \pm 84.2	189.7 \pm 71.3	0.5218 \pm 0.084
NI	0.5275 \pm 0.1521	0.2763 \pm 0.1172	333.6 \pm 95	174.7 \pm 73.4	0.5024 \pm 0.0841
II	0.5447 \pm 0.1528	0.2901 \pm 0.1202	344.9 \pm 95.5	183.6 \pm 75.3	0.511 \pm 0.0878
TI	0.5401 \pm 0.1422	0.2798 \pm 0.1189	341.6 \pm 88.5	176.8 \pm 74.3	0.4976 \pm 0.0884
SO	1.7037 \pm 0.3809	0.8224 \pm 0.2945	326.1 \pm 70.8	157.2 \pm 54.8	0.4699 \pm 0.0653
NO	1.4174 \pm 0.4569	0.6724 \pm 0.3106	271.2 \pm 84.7	128.5 \pm 57.8	0.4561 \pm 0.063
IO	1.6603 \pm 0.462	0.8204 \pm 0.338	318.3 \pm 85.6	157 \pm 62.6	0.4777 \pm 0.0668
TO	1.6327 \pm 0.423	0.7625 \pm 0.301	312.8 \pm 78.7	145.8 \pm 55.8	0.4531 \pm 0.063

N. Significance tables

Table S4. OCT videos significance table (preflight — postflight). Significance values for OCT videos measures comparisons between pre- and postflight.

	CT	Δ CT	LA	Δ LA	CVI	Δ CVI
global	0.01106	0.32039	0.00888	0.00885	0.16264	0.01097
NO	0.45268	0.01017	0.66394	0.26003	0.83872	0.04419
NI	0.12254	0.05423	0.06457	0.27618	0.09457	0.06929
C	0.01776	0.07849	0.01715	0.14034	0.03509	0.19580
TI	0.00254	0.82914	0.00609	0.09971	0.14367	0.11052
TO	0.00061	0.97176	0.00231	0.01703	0.08611	0.05197

Table S5. OCT volumes significance table (preflight — launch + 30 days). Significance values for OCT volumes measures comparisons between preflight and launch + 30 days.

	timepoint 1	timepoint 2	CV	LV	CT	LT	CVI
global	preflight	L + 30 days	1.028E-04	1.066E-04	8.388E-06	8.908E-05	0.00445
C	preflight	L + 30 days	9.181E-04	0.00167	7.114E-04	0.00145	0.00541
SI	preflight	L + 30 days	2.670E-04	5.728E-04	2.447E-04	5.220E-04	0.00471
NI	preflight	L + 30 days	2.024E-04	0.00126	1.616E-04	0.00110	0.02002
II	preflight	L + 30 days	1.965E-05	1.199E-04	1.284E-05	1.010E-04	0.00707
TI	preflight	L + 30 days	1.671E-04	4.341E-04	1.440E-04	3.882E-04	0.00586
SO	preflight	L + 30 days	3.590E-05	1.804E-04	2.778E-05	1.622E-04	0.00456
NO	preflight	L + 30 days	1.969E-05	3.935E-04	1.429E-05	4.058E-04	0.00972
IO	preflight	L + 30 days	3.641E-06	1.165E-05	5.952E-07	9.434E-06	0.00223
TO	preflight	L + 30 days	4.768E-05	4.054E-04	4.774E-05	4.574E-04	0.00740

Table S6. OCT volumes significance table (preflight — launch + 90 days). Significance values for OCT volumes measures comparisons between preflight and launch + 90 days.

	timepoint 1	timepoint 2	CV	LV	CT	LT	CVI
global	preflight	L + 90 days	3.076E-04	2.253E-04	1.918E-04	2.132E-04	2.163E-04
C	preflight	L + 90 days	3.176E-04	2.203E-04	3.365E-04	2.631E-04	7.060E-04
SI	preflight	L + 90 days	0.00167	0.00146	0.00144	0.00130	0.00210
NI	preflight	L + 90 days	3.171E-04	3.192E-04	2.383E-04	2.761E-04	3.084E-04
II	preflight	L + 90 days	2.211E-04	2.215E-04	1.550E-04	1.883E-04	2.705E-04
TI	preflight	L + 90 days	0.00108	9.589E-04	8.858E-04	8.058E-04	0.00232
SO	preflight	L + 90 days	6.941E-04	0.00116	4.953E-04	9.807E-04	0.00106
NO	preflight	L + 90 days	3.490E-05	6.333E-04	2.436E-05	7.673E-04	0.01964
IO	preflight	L + 90 days	6.734E-05	1.147E-04	5.159E-05	1.231E-04	1.180E-04
TO	preflight	L + 90 days	8.022E-04	0.00179	7.415E-04	0.00200	0.00128

Table S7. OCT volumes significance table (preflight — return - 30 days). Significance values for OCT volumes measures comparisons between preflight and return - 30 days.

	timepoint 1	timepoint 2	CV	LV	CT	LT	CVI
global	preflight	R - 30 days	0.02039	0.02692	0.01714	0.02535	0.03862
C	preflight	R - 30 days	0.03993	0.04456	0.03796	0.04544	0.11852
SI	preflight	R - 30 days	0.05337	0.06764	0.06204	0.07235	0.14100
NI	preflight	R - 30 days	0.01553	0.01836	0.01933	0.02099	0.02474
II	preflight	R - 30 days	0.01519	0.03136	0.01710	0.03214	0.10379
TI	preflight	R - 30 days	0.06583	0.11778	0.06932	0.11675	0.29263
SO	preflight	R - 30 days	0.03375	0.03672	0.03562	0.03930	0.06826
NO	preflight	R - 30 days	0.01369	0.02161	0.01616	0.02317	0.02350
IO	preflight	R - 30 days	0.00407	0.00751	0.00522	0.00849	0.01407
TO	preflight	R - 30 days	0.02994	0.03516	0.03137	0.03469	0.04026

Table S8. OCT volumes significance table (preflight — return + 1 to 3 days). Significance values for OCT volumes measures comparisons between preflight and return + 1 to 3 days.

	timepoint 1	timepoint 2	CV	LV	CT	LT	CVI
global	preflight	R + 1 to 3 days	0.00507	0.00215	6.422E-04	0.00393	0.14691
C	preflight	R + 1 to 3 days	0.00144	7.515E-04	0.00125	6.923E-04	0.00547
SI	preflight	R + 1 to 3 days	0.00200	0.00476	0.00160	0.00428	0.06474
NI	preflight	R + 1 to 3 days	0.00172	0.00412	0.00136	0.00350	0.10599
II	preflight	R + 1 to 3 days	5.467E-04	0.00145	4.809E-04	0.00144	0.03029
TI	preflight	R + 1 to 3 days	8.018E-04	0.00288	6.923E-04	0.00279	0.02137
SO	preflight	R + 1 to 3 days	0.00391	0.00691	0.00318	0.00915	0.14305
NO	preflight	R + 1 to 3 days	0.00567	0.01422	0.00661	0.02347	0.57548
IO	preflight	R + 1 to 3 days	2.992E-04	0.00152	1.370E-04	0.00408	0.27119
TO	preflight	R + 1 to 3 days	0.00197	0.00892	0.00339	0.01620	0.16142

Supplementary Information Bibliography

1. Rupesh Agrawal, Preeti Gupta, Kara-Anne Tan, Chui Ming Gemmy Cheung, Tien-Yin Wong, and Ching-Yu Cheng. Choroidal vascularity index as a measure of vascular status of the choroid: measurements in healthy eyes from a population-based study. *Scientific reports*, 6(1):21090, 2016.
2. Bjorn Kajun Betzler, Jianbin Ding, Xin Wei, Jia Min Lee, Dilraj S Grewal, Sharon Fekrat, Srinivas R Satta, Marco A Zarbin, Aniruddha Agarwal, Vishali Gupta, et al. Choroidal vascularity index: a step towards software as a medical device. *British Journal of Ophthalmology*, 106(2):149–155, 2022.
3. Xin Wei, Shozo Sonoda, Chitaranjan Mishra, Neha Khandelwal, Ramasamy Kim, Taiji Sakamoto, and Rupesh Agrawal. Comparison of choroidal vascularity markers on optical coherence tomography using two-image binarization techniques. *Investigative Ophthalmology & Visual Science*, 59(3):1206–1211, 2018.